TÜBİTAK

Turkish Journal of Earth Sciences

http://journals.tubitak.gov.tr/earth/

Research Article

Turkish J Earth Sci
(2019) 28: 661-670

doi:10.3906/yer-1902-10

GPS-derived source parameters of the 2014 North Aegean earthquake (Mw 6.9)

Aslı DOĞRU[1,*], Bahadır AKTUĞ[2], Fatih BULUT[1], Haluk ÖZENER[1]

[1]Department of Geodesy, Kandilli Observatory and Earthquake Research Institute, Boğaziçi University, İstanbul, Turkey
[2]Department of Geophysical Engineering, Faculty of Engineering, Ankara University, Ankara, Turkey

Received: 07.02.2019 • **Accepted/Published Online:** 26.06.2019 • **Final Version:** 04.09.2019

Abstract: We analyzed GPS data to investigate the source parameters of the 2014 North Aegean earthquake (Mw 6.9). We simultaneously inverted strike, dip, rake, average slip, moment, size, and location of the mainshock rupture using coseismic displacements. We also investigated static stress change associated with the mainshock and its influence on aftershock activity. Previous solutions of focal mechanism showed that mainshock has a nearly pure strike-slip nature. Our results also indicate that the mainshock has a right lateral strike-slip mechanism with a substantial extensional component. Average coseismic slips are 48 cm and 25 cm on the horizontal and vertical axis, respectively. Coseismic displacements reach up to 51.35 ± 4.55 mm at ~60 km from the hypocenter (LEMN station). It appears that the mainshock ruptured a fault section approximately 28 km deep and 70 km long and generated a stress drop along the ruptured segment ranging between 3 and 10 bar, with a stress increase of 3 bar at the edges of the rupture. Aftershocks were distributed to a broader area as coseismic stress increase affected a 200-km-long section of the western North Anatolian Fault.

Key words: 2014 North Aegean earthquake, GPS seismology, TUSAGA-Aktif (CORS-TR/Turkish RTK GPS network), coseismic displacement, geodesy, stress change

1. Introduction

Although modern seismic sensors have a large dynamic range, state-of-the-art broad-band seismometers could saturate even with moderately sized (M ≥ 6.0) earthquakes at distances close to the rupture (<50 km). On the other hand, GPS networks, which are comparatively less sensitive to relatively small events, operate in a noninertial frame and theoretically allow determination of displacements up to infinite wavelength. Static displacements obtained by GPS data could be used to invert for finite-source earthquake parameters. In this frame, we investigated the source parameters of the 2014 North Aegean earthquake (Mw 6.9) using a combined GPS network in the Aegean region.

Seismometer-derived fault plane solutions provide two nodal planes; the actual fault plane and the auxiliary plane. These solutions use a point-source model and provide two strikes, dips, and rakes defining the two nodal planes. Therefore, they cannot solely resolve a single fault plane. However, GPS observations provide the actual fault plane directly instead of specifying two nodal planes. This is because, GPS-derived fault plane solutions use a finite-dimension source model that defines length, widthdepth, and on-fault slip directly. In this study, we used GPS-derived coseismic displacements to simultaneously invert earthquake source parameters (strike, dip, rake, average slip, moment, size, and location of the mainshock rupture) (Table 1; Figure 1).

Static stress change associated with mainshock rupture substantially affects aftershock activity. Aftershocks are mostly distributed along the rupture zone and its close vicinity. In some cases, aftershocks might be distributed to a much broader area, as coseismic stress change might trigger ready-to-fail events at longer distances. In this context, we also investigated static stress change associated with the 2014 North Aegean earthquake and its influence on aftershock activity. This allowed us to understand the triggering mechanism for the aftershocks that have been activated at a substantial distance from the mainshock rupture.

1.1. North Aegean tectonics and the 2014 North Aegean earthquake

Active tectonics of the Aegean are driven by the subduction of the African lithosphere under the Aegean along the Hellenic Arc and the westward tectonic escape of Anatolia along the North Anatolian Fault System (McKenzie, 1972, 1978; Taymaz et al., 1991). The North Anatolian Fault (NAF) has a strong structural variation in the area,

* Correspondence: asli.dogru@boun.edu.tr

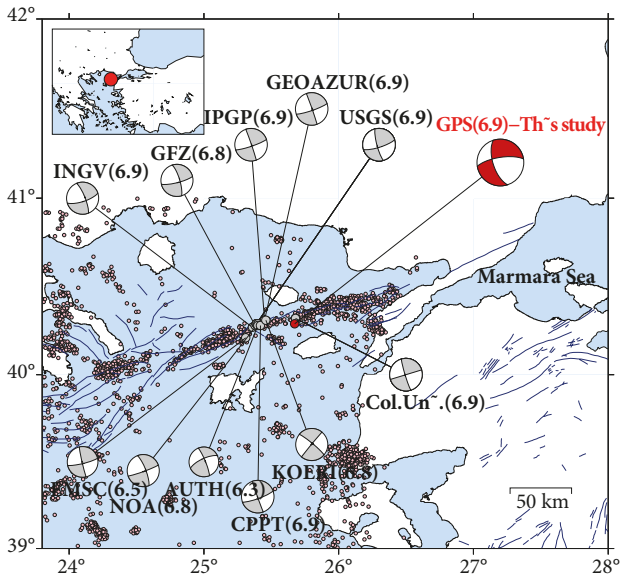

Figure 1. Focal mechanisms of the 2014 North Aegean earthquake (Mw 6.9) from this study (by GPS) and other sources. Pink dots show the earthquake epicenters refined by Bulut et al. (2018).

hosting mostly subparallel strike-slip segments with a significant amount of normal and reverse-type fault patches (Yaltırak and Alpar, 2002; McNeill et al., 2004), and it terminates in the western end of the North Aegean Trough (Pérouse et al., 2012; Chousianitis et al., 2015) (Figure 2).

The seismic gap between the 1975 and 1983 events was filled on May 24, 2014, by the North Aegean earthquake of Mw 6.9 (Figure 2) at the section of the NAF between the North Aegean and Saros basins. Previous studies have shown that the mainshock reactivated a ~90-km section of the NAF (Evangelidis, 2015; Saltogianni et al., 2015; Kiratzi et al., 2016; Bulut et al., 2018, Konca et al., 2018). However, it affected a ~200-km fault section according to the spatial distribution of the aftershocks. The fault plane had two major coseismic slip patches located beneath two prominent fault step-overs (Bulut et al., 2018). These strong structural offsets governed interseismic accumulation of the energy along the 2014 rupture zone and therefore generated an inhomogeneously distributed coseismic slip during the mainshock.

2. Data analysis

2.1. Inversion of source parameters using coseismic GPS displacements

We analyzed a network of 44 continuous GPS stations (13 from TUSAGA-Aktif/CORS-TR and 31 from the NOA Network) surrounding the North Aegean Sea. The distribution of sites is shown in Figure 3.

GPS data were processed using GAMIT/GLOBK software (Herring, 2004; King and Bock, 2004). IGS final orbit clock products and USNO Bull-B earth rotation parameters were utilized for the process. The effects of radiation pressure on the satellites were modeled in accordance with the Berne 9-parameter model. Both solid earth tide and ocean tide loading were applied by using the IERS 2003 model (McCarthy and Petit, 2004) and FES2004 (Letellier, 2004), respectively. Dry-part tropospheric errors were modeled by the Saastamoinen model (Saastamoinen, 1972) and the wet part was estimated from the data at 2-h intervals. The ionosphere-free model was used to remove the ionospheric effects.

Loosely constrained solutions were combined regardless of the datum definition of each contributing solution (Heflin et al., 1992; Blewitt, 1998). The daily repeatabilities of all sites were checked for a possible signature of the earthquake. Preearthquake and postearthquake periods of 15 days (GPS days: 129–159) were analyzed and the time series of station coordinates were obtained by GLOBK. The largest coseismic displacements were obtained at sites LEMN, CANA, ALEX, and IPSA (shown by bold black arrows in Figure 3).

We followed the procedure of Aktuğ et al. (2010) for the inversion method. As opposed to slip inversion, which poses a linear but ill-conditioned inversion problem where there is a large array of unknown slip patches with respect to the limited observations, geometry inver-

Table 1. Source parameters of the mainshock from this study (by GPS) and other sources.
a: Middle of fault; *b*: GEOAZUR Research Unit, France; *c*: USGS National Earthquake Information Service, Golden, CO, USA; *d*: European-Mediterranean Seismological Center, France; *e*: German Research Centre for Geosciences, Helmholtz Centre Potsdam, Germany; *f*: Lamont-Doherty Earth Observatory, Columbia University, NY, USA; *g*: Istituto Nazionale di Geofisica e Vulcanologia, Rome, Italy; *h*: The Institute of Earth Physics of Paris, France; *i*: Kandilli Observatory and Earthquake Research Institute, *İstanbul*, Turkey; *j*: National Observatory of Athens, Greece; *k*: French Polynesian Tsunami Warning Center, Papeete, Tahiti; *l*: Aristotle University of Thessaloniki, Greece.

Model	Long. (°)	Lat. (°)	Nodal plane 1			Nodal plane 2			Depth (km)	M_0 (dyn-cm)	Mw
			Strike (°)	Dip (°)	Rake (°)	Strike (°)	Dip (°)	Rake (°)			
This study (GPS) *a*	25.674	40.290	261	72	–153	-	-	-	28.1	3.33×10^{26}	6.94
GEOAZUR *b*	25.45	40.31	71	82	–178	341	88	–8	29	2.53×10^{26}	6.9
USGS *c*	25.39	40.29	165	79	13	72	77	168	6.4	2.56×10^{26}	6.9
EMSC *d*	25.31	40.21	167	87	9	76	81	177	25	6.32×10^{25}	6.5
GFZ *e*	25.38	40.28	343	76	–12	76	77	–164	20	2.10×10^{26}	6.8
Columbia Uni. *f*	25.68	40.32	163	85	0	253	90	–175	12	2.53×10^{26}	6.9
INGV *g*	25.36	40.27	72	73	–167	338	77	–18	20.5	2.40×10^{26}	6.9
IPGP *h*	25.45	40.31	341	88	-8	71	82	–178	29	2.53×10^{26}	6.9
KOERI *i*	25.46	40.31	219	88	173	309	83	1	24	1.54×10^{26}	6.8
NOA *j*	25.40	40.29	70	85	–167	338	77	–5	27	1.69×10^{26}	6.8
CPPT *k*	25.42	40.28	70	80	178	160	88	10	10	2.45×10^{26}	6.9
AUTH *l*	25.40	40.28	245	72	171	338	81	18	15	4.15×10^{25}	6.3

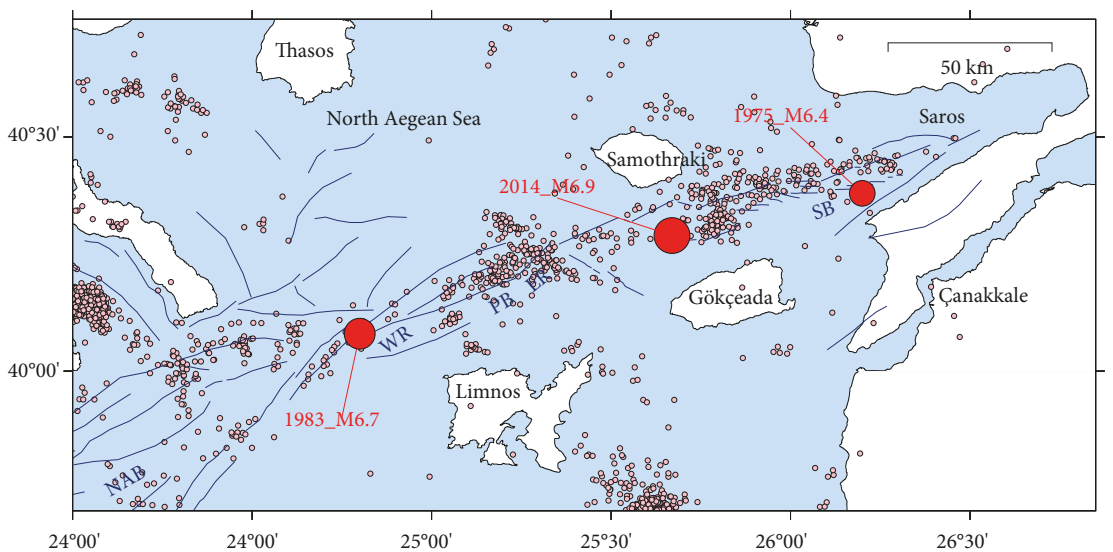

Figure 2. Pink dots represent seismicity between 2006 and 2014 (Bulut et al., 2018). Large red dot with black outline shows the epicenter of the 2014 mainshock (M 6.9). Blue bold lines are the active faults compiled by Bulut et al. (2018). Primary structural features mentioned in the text are the North Aegean Basin (NAB), the Western Ridge (WR), the Poseidon Basin (PB), the Eastern Ridge (ER), and the Saros Basin (SB).

sion of earthquake source parameters is a nonlinear and well-conditioned problem. For this reason, no smoothing/regularization is necessary for the inversion. On the other hand, geometry inversion is a global optimization problem that requires a method capable of avoiding local minima. Therefore, we employed simulated annealing for the geometry inversion. Coseismic GPS displacements were computed at 44 sites (Figure 3) and trend removal for

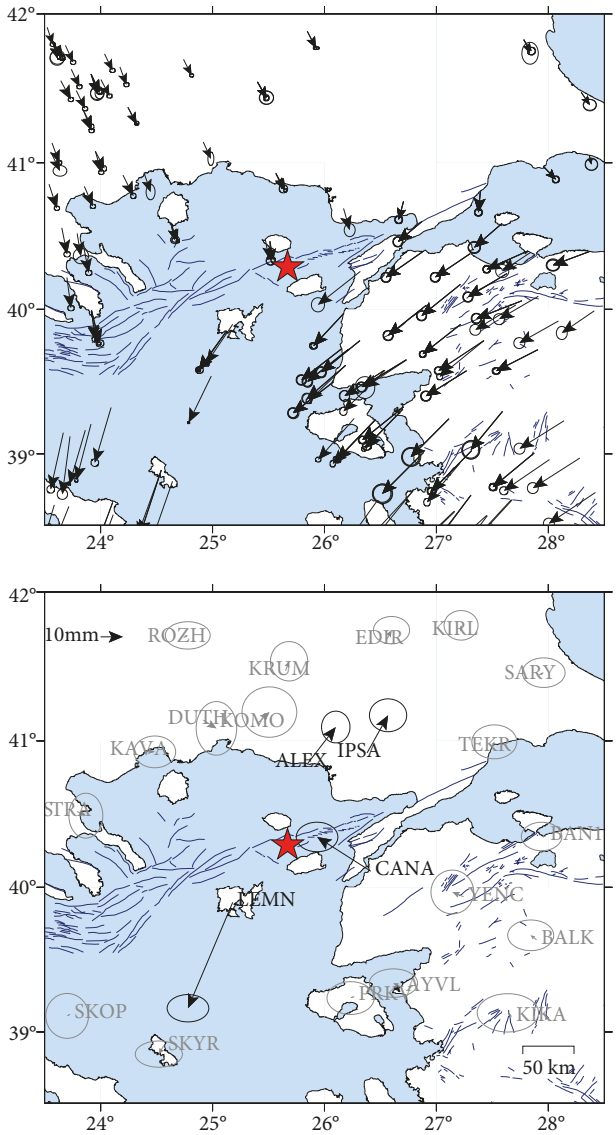

Figure 3. (a) Interseismic velocities by GPS (Kreemer et al., 2014). (b) Coseismic displacements by cGPS (this study). Star represents the mainshock of the 2014 North Aegean earthquake (Mw 6.9).

interseismic correction was performed in the time series for each computed displacement. The maximum horizontal displacement was obtained at the nearest GPS station, LEMN (Figure 3). The time series of the closest sites are shown in Figure 4. The coseismic GPS displacements and misfits are given in Table 2.

Following Okada (1985), coseismic displacements were initially modeled as displacements at a free surface due to a dislocation in elastic half-space. In a second step, this initial model was improved, inverting coseismic displacements and slips simultaneously. An inversion schema was designed to minimize the weighted residual sum of squares (wrss) between observed and theoretical displacements.

It is critical to define a proper initial model for iterative inversion to reasonably converge the model parameters, especially in the case of linearly dependent datasets (nonevenly distributed layout of GPS stations). A complex relation between surface displacements and fault geometry results in potentially many local minima. The optimization was performed using a simulated annealing approach to avoid local minima (Kirkpatrick, 1983). Although this approach is useful to avoid converging on local minima, it has limitations to reasonably converge to global minimum. Therefore, simulated annealing-derived results were refined in a second step using the Broyden–Fletcher–Goldfarb–Shanno (BFGS) algorithm. The observed and modeled displacements are summarized in Figure 5. As provided in Table 2 and Figure 3, stations at distances of more than ~100 km from the rupture accommodate insignificant coseismic offsets. On the other hand, coseismic offsets closer to the rupture are statistically significant, while at those sites, the difference between the modeled and observed offsets is statistically insignificant.

Considering the earthquake magnitude and the observed displacements, we did not expect significant postseismic displacements larger than the uncertainties of the coseismic offsets. Furthermore, since the coseismic offsets were derived from data only 1 day before/after the earthquake epoch, they are practically free from any postseismic effect. No nonlinearity was observed in the time series following the earthquake. This is also an indication of insignificant postseismic displacements in our time series during the period of interest.

We sampled observation errors of the displacements 100 times from a normal distribution using the original data covariance structure. The inversion was repeated for each reconstructed set of observations and a different set of the initial parameters. This approach allows the assessment of the error bounds of the parameters as well as the trade-offs between model parameters (Figure 6). For instance, the average uncertainty of strike was about ±10° while it was about ±5° for the dip. The upper limit of the slip was fixed at 1 m. Moment was used to improve the stability of the inversion, although it was dependent on width and length of the rupture area, e.g., a wider rupture might result in a larger moment magnitude, or vice versa.

The obtained fault geometry and slip values are given in Table 3. Our results show that the mainshock has a right lateral strike-slip mechanism with a substantial extensional component. Average coseismic slip is 48 cm on the horizontal axis and 25 cm on the vertical axis. Coseismic displacements range between 0.22 mm and 51.35 mm at distances of ~323 km and ~60 km from the mainshock hypocenter, respectively.

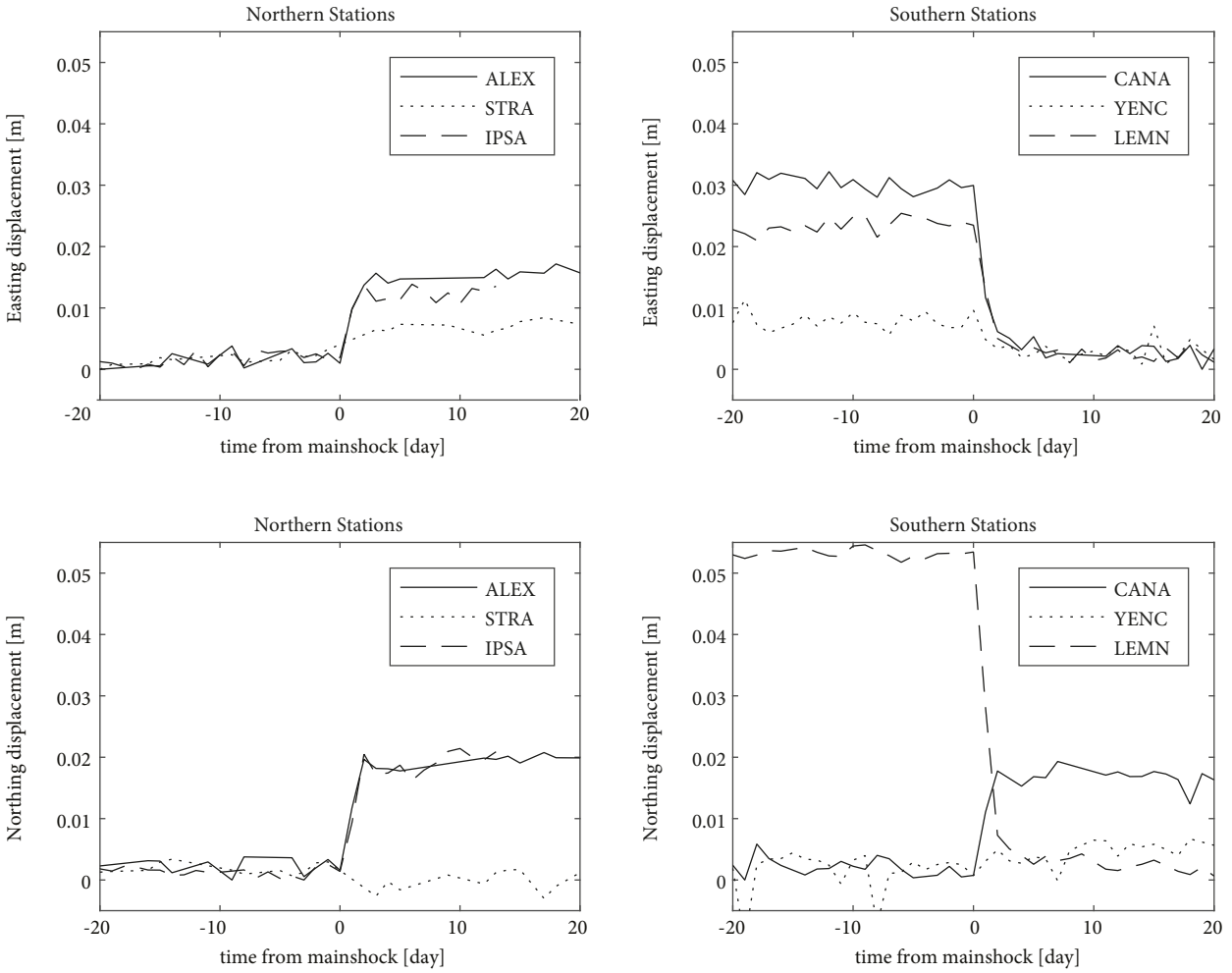

Figure 4. GPS time series of the nearest 6 stations: ALEX, STRA, IPSA, CANA, YENC, and LEMN.

2.2. Coulomb stress change and aftershocks

Characterizing the relationship between the mainshock and the aftershocks is fundamental to understanding the mechanism of postearthquake processes. In this context, we analyzed Coulomb stress change during the mainshock of the 2014 North Aegean earthquake (Mw 6.9) to investigate static stress change associated with the mainshock and its correlation with aftershock distribution. In principle, Coulomb stress change is not sensitive to the regional stress field. However, it is a function of fault geometry, slip, friction coefficient, and elastic properties of the earth's crust (Toda et al., 2011). In this context, we assumed elastic half-space with a shear modulus of 32 GPa (earth's crust) and a Poisson's ratio of 0.25.

We tested both single-segment and two-segmented rupture models (Figure 7). The single-segment model is based on our source parameter calculations. The two-segmented model, however, is based on the coseismic model of Bulut et al. (2018). We compared our stress change calculations with early aftershocks (Bulut et al., 2018). Both models verified that the aftershocks appear more on the stress-increase sections of the NAF in the vicinity of the 2014 rupture. Stress-decrease sections also accommodated aftershock activity. There were two subsidiary faults that remain in stress-decrease areas. According to the present results and the results of previous studies, although the rupture length is less than 90 km (±45 km from the mainshock hypocenter), the mainshock triggered aftershock activity at a distance of ~100 km from the mainshock hypocenter in the west, far beyond the 2014 rupture (Saltogianni et al., 2015; Kiratzi et al., 2016; Bulut et al., 2018). Our calculations indicate that this remote triggering can be attributed to the Coulomb stress change associated with the 2014 mainshock (Figure 7), among other factors, such as those from dynamic loading due to the passage of seismic waves.

Table 2. Observed and modeled coseismic displacements.

Site	Lon. (°)	Lat. (°)	Observed				Modeled			
			de (mm)	dn (mm)	sde (mm)	sdn (mm)	de (mm)	dn (mm)	sde (mm)	sdn (mm)
AFYT	23.435	40.097	1.1	–0.8	3.5	3.2	–0.57	–1.87	1.41	1.26
ALEX	25.853	40.849	12.4	16.1	2.6	2.9	15.65	13.43	1.04	1.14
ANDR	24.737	37.886	–3.1	–6.0	5.4	5.7	–1.23	–1.85	2.16	2.29
AYVL	26.686	39.311	–3.5	1.8	4.4	2.6	–4.94	4.17	1.76	1.02
BALK	27.894	39.639	–2.6	2.0	4.2	2.8	–2.08	1.89	1.67	1.12
BAN1	27.975	40.349	–1.8	0.0	3.7	2.6	0.66	1.77	1.48	1.03
BURG	27.468	42.500	0.3	0.4	3.4	2.7	1.47	1.96	1.35	1.09
CANA	26.414	40.111	–24.0	15.3	3.8	2.7	–16.66	15.83	1.51	1.09
CESM	26.373	38.304	–0.1	–0.8	4.6	2.3	–1.29	0.16	1.85	0.90
CHIO	26.127	38.368	–0.5	0.1	3.1	2.9	–1.35	–0.36	1.24	1.15
DUTH	24.917	41.140	5.9	–3.7	3.7	4.9	8.29	–8.18	1.46	1.97
EDES	22.051	40.804	–0.2	–1.7	4.1	4.5	0.73	–0.76	1.65	1.81
EDIR	26.551	41.677	2.4	4.5	3.3	2.5	3.55	5.00	1.32	0.98
ELH1	26.583	42.177	2.5	1.9	2.7	2.4	1.89	2.71	1.09	0.95
IPSA	26.380	40.918	9.4	16.8	3.4	3.0	14.40	17.67	1.36	1.20
IZMI	27.082	38.395	–1.1	–0.1	3.6	3.2	–1.51	1.17	1.45	1.26
KAVA	24.387	40.934	4.9	–0.6	3.8	2.9	8.69	–7.01	1.53	1.17
KIKA	27.672	39.106	–1.7	1.7	5.6	3.5	–2.44	2.05	2.22	1.39
KIRL	27.218	41.738	0.1	2.6	3.1	2.7	3.15	3.86	1.24	1.06
KLOK	22.014	39.565	–0.2	0.1	4.4	2.6	–0.63	–0.80	1.74	1.03
KOMO	25.406	41.120	5.1	4.9	5.0	4.6	7.45	–3.65	1.99	1.84
KRUM	25.652	41.473	1.6	4.2	3.4	3.6	3.57	1.86	1.36	1.44
KUST	22.713	42.284	0.2	–0.2	3.6	2.4	1.16	–1.01	1.45	0.96
LARI	22.388	39.614	–0.9	–0.6	3.2	3.8	–0.82	–1.00	1.27	1.52
LEMN	25.181	39.897	–20.0	–47.3	3.8	2.5	–34.58	–44.39	1.51	0.99
NOA1	23.864	38.047	–1.2	–6.3	4.4	4.7	–1.52	–2.00	1.76	1.86
PANG	24.174	42.514	–0.1	0.5	3.8	3.4	1.21	–1.01	1.50	1.36
PLOV	24.759	42.162	1.9	0.1	5.4	3.2	1.63	–1.10	2.16	1.27
PRKV	26.265	39.246	–1.6	–0.7	4.3	3.0	–4.38	2.01	1.71	1.20
PROV	23.387	41.068	2.5	–0.4	3.1	3.6	2.79	–2.15	1.23	1.42
PTOL	21.678	40.511	1.1	0.2	4.1	2.8	0.33	–0.60	1.62	1.10
ROZH	24.741	41.696	1.9	0.9	4.1	2.5	3.02	–2.68	1.62	1.00
SARY	27.916	41.443	2.1	1.1	3.9	2.7	2.77	2.72	1.56	1.06
SERR	23.037	41.286	1.4	–2.5	4.3	6.5	2.05	–1.61	1.73	2.60
SKOP	23.728	39.122	–1.3	–0.7	3.9	4.1	–3.30	–3.33	1.56	1.65
SKYR	24.565	38.904	–2.2	–3.8	4.3	2.4	–3.96	–5.32	1.72	0.94
SLIV	26.341	42.673	2.2	0.1	5.1	3.4	1.09	1.45	2.02	1.36
SOFI	23.395	42.556	0.5	–0.2	3.8	2.3	1.13	–1.03	1.52	0.93
STEF	22.743	39.464	0.2	0.4	3.5	2.3	–1.33	–1.35	1.38	0.90
STRA	23.791	40.520	3.9	–1.9	3.1	4.1	2.88	–2.71	1.25	1.62
TEKR	27.497	40.958	1.0	2.3	4.1	3.1	4.53	4.10	1.63	1.23
THS1	22.959	40.627	2.4	–0.9	3.3	2.8	1.25	–1.32	1.31	1.10
VOLO	22.887	39.353	–0.6	–0.9	3.3	2.6	–1.62	–1.57	1.32	1.03
YENC	27.242	39.936	–5.0	2.1	3.9	4.0	–3.56	3.63	1.56	1.61

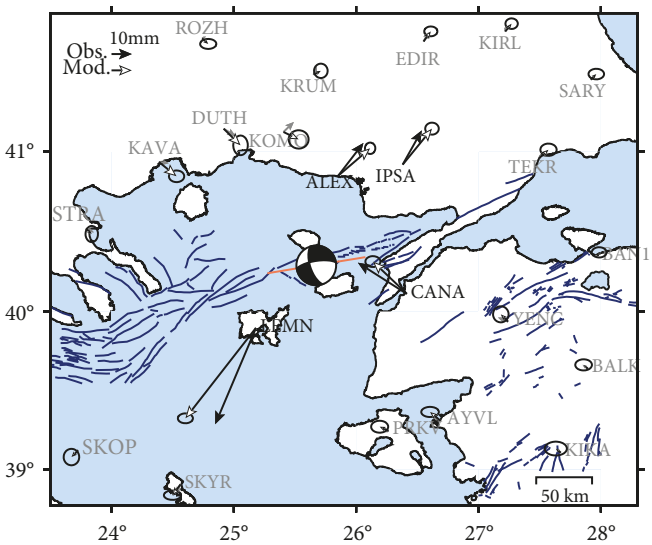

Figure 5. GPS station distribution used for the analysis of the earthquake source and misfits. Orange solid line represents the rupture of the 2014 North Aegean earthquake (Mw 6.9).

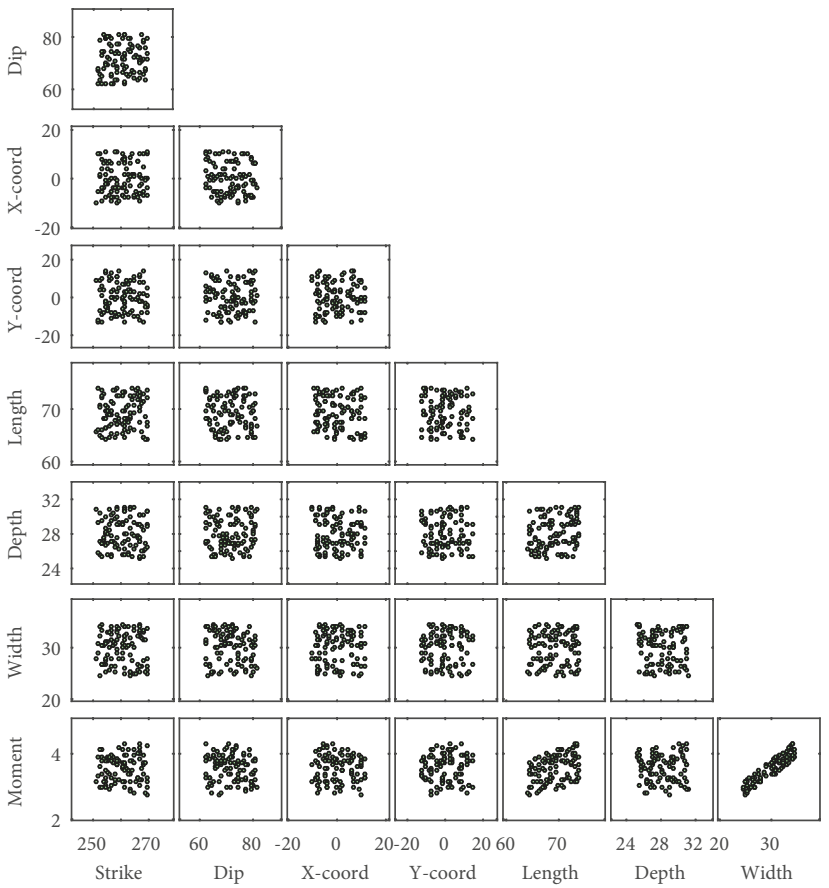

Figure 6. Trade-offs between source/model parameters. Unit of the strike and dip is degree, moment is $\times 10^{26}$ dyne-cm, and all other parameters are in kilometers. The X-coordinate and Y-coordinate are along the east and the north direction, respectively, and with respect to the reference point at 40.290°N, 25.674°E.

Table 3. Inverted parameters by GPS finite source.

Lon-1 (°)	Lat-1 (°)	Lon-2 (°)	Lat-2 (°)	Azimuth (°)	Dip (°)	Length (km)	Width (km)	Depth (km)	Strike-slip (m)	Dip slip (m)
26.075	40.341	25.274	40.240	261.1	71.7	69.05	29.52	28.1	–0.48	–0.25

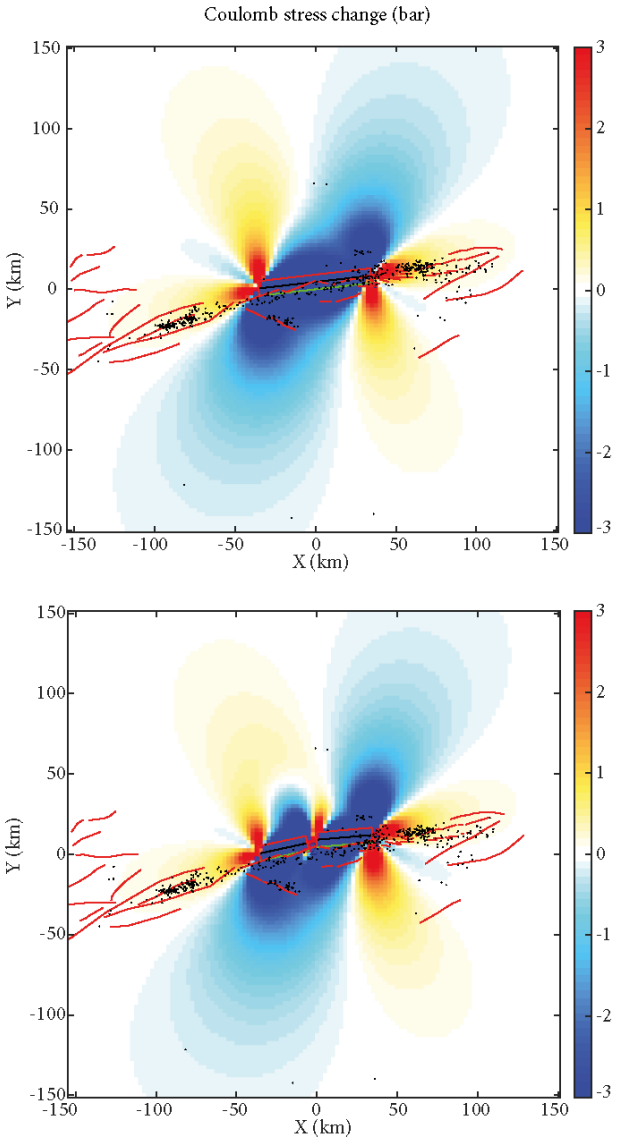

Figure 7. Coulomb stress change associated with the mainshock. Upper panel: a single-segment rupture model; lower panel: two-segmented rupture model. Black dots represent aftershock epicenters.

3. Discussion and conclusions

Seismological data have been previously used to determine kinematic source parameters of the 2014 North Aegean earthquake (Mw 6.9). The studies given in Table 1 and Figure 1 indicate that the mainshock is connected with strike-slip motion along a steeply dipping fault plane that strikes ENE-WSW in accordance with the geometry of the NAF. In this study, we used absolute near-field GPS displacements to simultaneously obtain location, size, slip, and kinematic source parameters. According to our results, the 2014 North Aegean earthquake occurred at a latitude of 40.290°N and a longitude of 25.674°E with a magnitude of 6.94 at a depth of 28.1 km. The geodetic moment was found to be 3.33×10^{26} dyne-cm, comparable to the seismic calculations. The focal mechanism of the mainshock, as obtained from our inversion, is in accordance with previously published solutions regarding the dextral strike-slip motions. However, our solution has a more significant dip slip component compared to previous studies. Correspondingly, we found on-fault average coseismic slip as 48 cm and 25 cm on the lateral and vertical axis, respectively.

On-fault slip of the 2014 North Aegean earthquake has been previously modeled using different approaches, such as back-projection of strong-motion waveforms (Evangelidis, 2015), joint analysis of GPS and teleseismic seismograms (Saltogianni et al., 2015), teleseismic seismograms (Kiratzi et al., 2016), and coseismic GPS measurements (Bulut et al., 2018; Konca et al., 2018). The models verified that the 2014 mainshock failed two subsegments, excluding the three-segmented model by Konca et al. (2018). The models indicate that the rupture length might range from 60 to 95 km (~85 km by Evangelidis, 2015; ~60 km by Saltogianni et al., 2015; ~95 km by Kiratzi et al., 2016; ~90 km by Bulut et al., 2018; ~90 km by Konca et al., 2018). These previous investigations broadly focused on the dextral fault slip, though some of them considered the dip slip component as well. On the other hand, the GPS-derived model from this study focuses more on the dip slip component.

The results of this study reveal that on-land coseismic displacements reach up to 51.35 ± 4.55 mm at ~60 km from the hypocenter (LEMN station). The mainshock ruptured a fault section 70 km long. It is interesting to note that the rupture extends down to a depth of ~28 km at the lower crust, near the Moho. The mainshock is associated with a stress drop between 3 and 10 bar along the ruptured segment and a stress increase of 3 bar at the edges of the rupture. In the west, far beyond the 2014 rupture, there is a prominent cluster of earthquakes (24.10°E to 24.30°E), presumably triggered by the mainshock. Al-

though the rupture should be at most 90 km long (45 km in the east and 45 km in the west), this cluster is located at a distance of ~100 km from the mainshock (Figure 7). This remote triggering has also been observed on many other occasions, e.g., the triggering of the Çerkeş cluster at ~240 km from the 1999 İzmit mainshock (Utkucu et al., 2003). Basically, triggering an earthquake requires increasing shear stress or decreasing fault normal stress on the plane of the fault patch accommodating the potentially triggered earthquake. Mostly, these types of remote triggering occur in the event that the earthquakes are ready-to-fail, as coseismic change of Coulomb stress can be only a very few bars at such long distances. In our case, there is an increase of ~1 bar of Coulomb stress change along this westernmost cluster. It appears that aftershocks are distributed to a broader area as coseismic stress increase affected a ~200-km-long section of the western North Anatolian Fault.

Acknowledgments
GPS data were obtained from the Bulgarian Academy of Sciences and the Turkish RTK GPS Network. The authors thank Ivan Georgiev for providing GPS data. The authors would also like to thank Tulay Kaya Eken for proofreading the manuscript. A GMT mapping tool (Wessel et al., 2013) and MATLAB were used to generate maps and graphs.

References

Aktuğ B, Kaypak B, Çelik RN (2010). Source parameters for the Mw = 6.6, 03 February 2002, Çay Earthquake (Turkey) and aftershocks from GPS, Southwestern Turkey. Journal of Seismology 14: 445. doi.org/10.1007/s10950-009-9174-y

Blewitt G (1998). GPS data processing methodology: from theory to applications In: Teunissen PJG, Kleusberg A (editors). GPS for Geodesy. New York, NY, USA: Springer-Verlag, pp. 231-270.

Bulut F, Özener H, Doğru A, Aktuğ B, Yaltırak C (2018). Structural setting along the Western North Anatolian Fault and its influence on the 2014 North Aegean Earthquake (Mw 6.9). Tectonophysics 745: 382-394. doi: 10.1016/j.tecto.2018.07.006

Chousianitis K, Ganas A, Evangelidis CP (2015). Strain and rotation rate patterns of mainland Greece from continuous GPS data and comparison between seismic and geodetic moment release. Journal of Geophysical Research Solid Earth 120: 3909-3931. doi: 10.1002/2014JB011762

Evangelidis C (2015). Imaging supershear rupture for the 2014 Mw 6.9 Northern Aegean earthquake by backprojection of strong motion waveforms. Geophysical Research Letters 42: 307-315. doi: 10.1002/2014GL062513

Heflin MB, Bertiger WI, Blewitt G, Freedman AP, Hurst KJ et al. (1992). Global geodesy using GPS without fiducial sites. Geophysical Research Letters 19: 131-134.

Herring TA (2004). GLOBK: Global Kalman Filter VLBI and GPS Analysis Program. Cambridge, MA, USA: Massachusetts Institute of Technology.

King RW, Bock Y (2004). Documentation of the MIT GPS Analysis Software: GAMIT. Cambridge, MA, USA: Massachusetts Institute of Technology.

Kiratzi A, Tsakiroudi E, Benetatos C, Karakaisis G (2016). The 24 May 2014 (Mw6.8) earthquake (North Aegean Trough): spatiotemporal evolution, source and slip model from teleseismic data. Physics and Chemistry of the Earth 95: 85-100. doi: 10.1016/j.pce.2016.08.003

Kirkpatrick S, Gelatt CD Jr, Vecchi MP (1983). Optimization by simulated annealing. Science 220 (4598): 671-680.

Kreemer C, Blewitt G, Klein EC (2014). A geodetic plate motion and Global Strain Rate Model. Geochemistry, Geophysics, Geosystems 15: 3849-3889. doi: 10.1002/2014GC0054 07

Konca AO, Cetin S, Karabulut H, Reilinger R, Dogan U et al. (2018). The 2014, M W6.9 North Aegean earthquake: seismic and geodetic evidence for coseismic slip on persistent asperities. Geophysical Journal International 213 (2): 1113-1120.

Letellier T (2004). Etude des ondes de marée sur les plateux continentaux. PhD, Université de Toulouse III, Toulouse, France (in French).

Loveless JP, Meade BJ (2011). Spatial correlation of interseismic coupling and coseismic rupture extent of the 2011 Mw = 9.0 Tohoku-Oki earthquake. Geophysical Research Letters 38: L17306. doi: 10.1029/2011GL048561

McCarthy DD, Petit G (2004). IERS Conventions (2003). IERS Technical Note 32. Frankfurt, Germany: Verlag des Budesamts fur Kartographie und Geodasie.

McKenzie DP (1972). Active tectonics of the Mediterranean region. Geophysical Journal of the Royal Astronomical Society 30: 109-185.

McKenzie DP (1978). Active tectonics of the Alpine Himalayan Belt, the Aegean Sea and surrounding regions. Geophysical Journal of the Royal Astronomical Society 55: 217-252.

McNeill LC, Mille A, Minshull TA, Bull JM, Kenyon NH et al. (2004). Extension of the North Anatolian Fault into the North Aegean Trough: evidence for transtension, strain partitioning, and analogues for Sea of Marmara basin models. Tectonics 23 (2): TC2016. doi: 10.1029/2002TC001490

Meade BJ, Hager BH (2005). Block models of crustal motion in southern California constrained by GPS measurements. Journal of Geophysical Research: Solid Earth 110: B3.

Moreno M, Rosenau M, Oncken O (2010). 2010 Maule earthquake slip correlates with pre-seismic locking of Andean subduction zone. Nature 467 (7312): 198-202. doi: 10.1038/nature09349

Okada Y (1985). Surface deformation due to shear and tensile faults in a half-space. Bulletin of the Seismological Society of America 75 (4): 1135-1154.

Pérouse E, Chamot-Rooke N, Rabaute A, Briole P, Jouanne F et al. (2012). Bridging onshore and offshore present-day kinematics of central and eastern Mediterranean: Implications for crustal dynamics and mantle flow. Geochemistry, Geophysics, Geosystems 13: Q09013. doi: 10.1029/2012GC004289

Saastamoinen J (1972). Atmospheric correction for the troposphere and stratosphere in radio ranging of satellites. In: Henriksen SW, Mancini A, Chovitz BH (editors). The Use of Artificial Satellites for Geodesy. Geophysical Monograph Series (15). Washington, DC, USA: AGU, pp. 247-251.

Saltogianni V, Gianniou M, Taymaz T, Yolsal-Çevikbilen S, Stiros S (2015). Fault slip source models for the 2014 Mw 6.9 Samothraki-Gökçeada earthquake (North Aegean trough) combining geodetic and seismological observations. Journal of Geophysical Research 120 (12): 8610-8622. doi: 10.1002/2015JB012052

Savage JC (1983). A dislocation model of strain accumulation and release at a subduction zone. Journal of Geophysical Research: Solid Earth 88 (B6): 4984-4996.

Taymaz T, Jackson JA, McKenzie D (1991). Active tectonics of the North and Central Aegean Sea. Geophysical Journal International 106: 433-490.

Toda S, Stein RS, Sevilgen V, Lin J (2011). Coulomb 3.3 Graphic-Rich Deformation and Stress-Change Software for Earthquake, Tectonic, and Volcano Research and Teaching—User Guide. U.S. Geological Survey Open-File Report 2011–1060. Reston, VA, USA: USGS.

Utkucu M, Alptekin Ö, Pınar A (2003). A detailed source study of the Orta (Çankırı) earthquake of June 6, 2000 (M_S = 6.1): an intraplate earthquake in central Anatolia. Journal of Seismology 7 (2): 193-202.

Wessel P, Smith WHF, Scharroo R, Luis JF, Wobbe F (2013). Generic mapping tools: improved version released EOS Trans. AGU 94 (45): 409-410.

Yaltırak C, Alpar B (2002). Kinematics and evolution of the northern branch of the North Anatolian Fault (Ganos Fault) between the Sea of Marmara and the Gulf of Saros. Marine Geology 190 (1-2): 351-366.